MATERIALS
CHEMISTRY
FRONTIERS

Check for updates

Dual-template approach to hierarchically porous polymer membranes†

Thomas J. F. Southern [iD] and Rachel C. Evans [iD] *

The non-solvent induced phase separation (NIPS) method is often used to fabricate porous polymer membranes that have a wide variety of applications in the fields of purification and energy materials. Such applications typically require membranes with a well-controlled pore structure across multiple levels of structural hierarchy. However, with the NIPS method, the membrane porosity is typically restricted to a single structural level due to the use of just one type of templating agent, commonly a polymer amphiphile. To overcome this limitation, here we report a new dual-template approach to embed multilevel porosity into poly(ethersulfone) membranes. In this approach, the polymer amphiphile Pluronic® F127 (F127) is used to template the higher level structure (10 μm scale), while a secondary molecular template, 4-(phenyl)azobenzoic acid (PABA), is simultaneously introduced to enable structural control at the 1 μm level. Analysis of the membrane structure by scanning electron microscopy revealed that F127 creates larger finger-like pores, while PABA introduced a more fibrous, interconnected porous sub-structure. Contact angle measurements showed that the PABA additive increases the hydrophilicity of the resultant membranes, while dead-end permeability measurements demonstrated that the hierarchical pore structure results in a 95% increase in permeability compared to a single level pore structure. Solvent extraction studies revealed that quantitative removal of the PABA template could be achieved, without any modification to the secondary level pore structure. This process offered the benefit of removing flakes of crystallized PABA from the larger, finger-like pores, leading to a further 300% increase in permeability. Given the simplicity and versatility of the NIPS method, this dual-template approach presents an efficient route to hierarchically structured, porous polymer membranes whose properties may be tailored for a targeted application.

Introduction

Polymer membranes find application in a wide variety of fields from energy materials to water purification.[1–6] These applications often require a well-controlled internal pore structure in order to allow membrane properties such as pore connectivity and surface area to be finely tuned.[7] For most purposes, a high fluid throughput for a given pore size is desirable.[8] To this end, the microstructure of the membrane must be controlled to maximize pore connectivity and thus flow rate, whilst allowing the rejection ratios of contaminants per effective surface area of the membrane to be maintained. A common challenge is achieving this combination of desired properties at a suitable price point, due to the need for facile manufacturing methods.[9]

Poly(ethersulfone) (PES) is frequently used as a membrane material as due to its high glass-transition temperature

(225 °C[9]), large working pH range (3–10[10]) and high-pressure resistance (25 bar[11]). PES membranes are typically prepared using the non-solvent induced phase separation method (NIPS), as it is easy to accomplish on a large scale, using green manufacturing conditions through ambient processing.[5,12,13] In the NIPS method, the polymer is first dissolved in a good solvent, after which the solution is immersed in a non-solvent to induce precipitation of a thin film.[14–19] Polymeric surfactants such as Pluronic® F127 (F127),[14,20,21] Tween-20[22] or Tetronic 1307[23,24] are commonly added to the precursor solution to template pore formation in the final membrane. The conditions of the precursor solution induce the formation of surfactant micelles, which act to stabilize the developing pores during phase inversion.[20,25] Multiple micelles can form in the pores leading to a change in the affinity between the non-solvent and solvent, affecting the speed of membrane formation and the resultant microstructure.[20] This micelle formation leads to a larger, more well-defined pore structure at the 10 μm level, when compared with membranes not including a surfactant additive.[20] This is typically observed as a microstructure of vertical, finger-like pores, that broaden slightly through the

Department of Materials Science & Metallurgy, University of Cambridge, 27 Charles Babbage Road, Cambridge CB3 0FS, UK. E-mail: rce26@cam.ac.uk

† Electronic supplementary information (ESI) available: Histograms from SEM analysis showing pore size distributions. See DOI: 10.1039/d0qm00610f

membrane thickness, below a more dense skin layer.[20] This skin layer predominantly contain pores on a sub-micron scale. We note that smaller mesopores, on the length scales typically observed for mesoporous inorganic oxides prepared using F127,[26,27] may be present in this skin layer. The amphiphilic nature of the surfactants also increases the surface hydrophilicity of the membrane, an important factor in preventing biofouling of the membrane surface and thus maintaining operational performance.[20,21,28,29] However, while this approach leads to larger pores and thus higher permeability compared to non-templated analogues,[14,30,31] the effect on pore connectivity at the sub-micron level is still poorly understood.

To overcome this limitation, here we present a new dual template approach to introduce hierarchical porosity into PES membranes fabricated using the NIPS method. The top-level (10 μm) pore structure is still controlled by the polymeric surfactant F127, while the small molecule 4-(phenylazo)benzoic acid (PABA) introduces an additional level of structural hierarchy at the 1 μm scale, to improve pore connectivity. PABA was chosen as the additive due to its size and the availability of a terminal carboxyl acid group to facilitate favourable dipolar interactions with PES. Moreover, its bright orange coloration facilitates easy tracking of its elimination from the membrane and its potential recovery for use in future synthesis to prevent waste in adherence with green chemistry principles.[32] We use scanning electron microscopy (SEM) to examine the microstructure of membranes in which the small molecule template is retained or post-synthetically removed. Dead-end permeability testing and water contact angle measurements are then used to correlate the membrane properties with the microstructure.

Experimental

Materials

Ultrason® E 6020 P poly(ethersulfone) (M_w = 75 000 g mol^{-1}) was purchased from BASF and dried at 100 °C overnight, before use, to remove adsorbed water. N,N-Dimethylformamide (DMF, AnalR grade) and ethanol (Absolute 99.8+%, certified AR for Analysis) were purchased from Fisher Scientific Ltd and were used as received. 4-(Phenylazo)benzoic acid (98%) and Pluronic® F-127 (M_w = 12 600 g mol^{-1}) were purchased from Sigma Aldrich and used as received. The structures of these reagents are presented in Fig. 1a. Deionized water, with resistivity between 1 MΩ cm and 10 MΩ cm, was produced using a Purite Select Fusion water purification system.

Membrane preparation by non-solvent induced phase separation

A schematic representation of the NIPS method, which was used to produce the polymer membranes described in this work is shown in Fig. 1b. Control samples were prepared by dissolving in DMF (73 wt%) the membrane material, PES (18 wt%) and F127 (9 wt%), as a primary pore-former and surface-modifying agent. Test samples were prepared by adding PABA as a nanostructure-altering agent (PES – 18 wt%, F127 – 9 wt%, PABA – 15 wt%, DMF – 57 wt%). For both test and control samples, the solutions were stirred at 70 °C for around an hour until all components were completely dissolved and the sample had reached a homogenous, pourable viscosity. Small and large membranes were prepared as outlined below.

Glass substrates (50 mm × 75 mm, or 101 mm × 153 mm) were prepared by coating the edges with two layers of masking tape. The membrane solution was spread between the masking tape edges using a glass rod to a wet thickness of ca. 300 μm. The samples were then left in a desiccator at a humidity below 30% for 15 minutes to allow any trapped gas bubbles to escape. The samples were then fully immersed into deionised water at room-temperature, by suspending them from a clamp and raising the immersion bath from below with a lift such that the sample remained horizontal through immersion. The solution transformed into a solid film within the first 5 seconds of immersion into the water. The solid films were left immersed
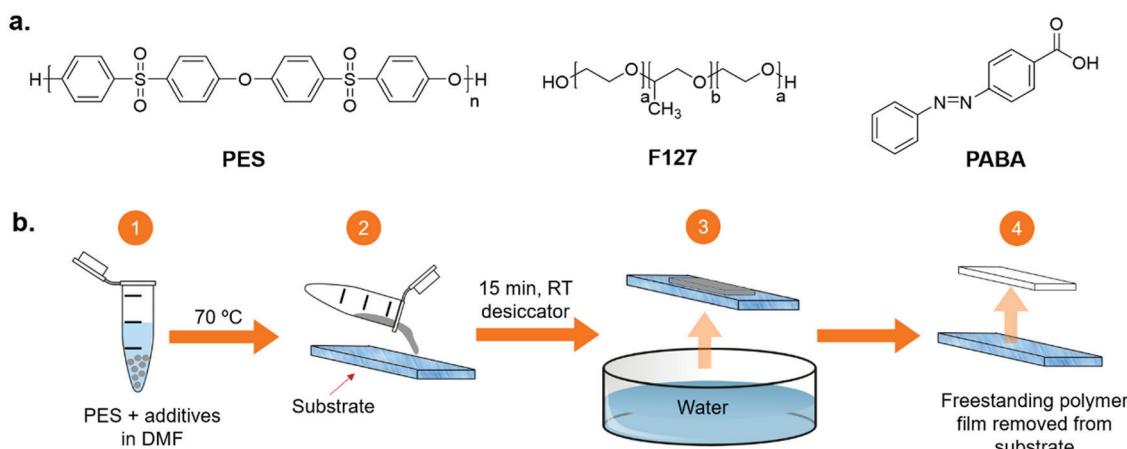
Fig. 1 (a) Chemical structures of poly(ethersulfone) (PES), Pluronic® F-127 (a = 101, b = 56) (F127) and 4-(phenylazo)benzoic acid (PABA). (b) Schematic diagram of the non-solvent induced phase separation process for membrane manufacture. (1) Solution of PES, F127, and optional PABA, in DMF heated to 70 °C. (2) Solution poured onto prepared glass substrate, stored in desiccator for 15 minutes. (3) Coated substrate fully immersed in water. (4) Solid product membrane is removed from substrate.

784 | Mater. Chem. Front., 2021, **5**, 783–791

This journal is © The Royal Society of Chemistry and the Chinese Chemical Society 2021

for approximately 4 minutes, before being removed from their substrates by hand and transferred to Petri dishes where they were stored in deionised water until characterisation.

Scanning electron microscopy (SEM)

The cross-sectional microstructure of the membranes was analysed by SEM. Samples were prepared by freeze-cracking in liquid nitrogen and coating in palladium using an Emtech K575 sputter coater. Samples were mounted on 90° SEM stubs, using carbon paste, such that their cross-section could be viewed using 0° tilt. SEM analysis was performed using a Thermo Scientific™ Phenom ProX scanning electron microscope. SEM analysis was used to determine the pore sizes of the skin layer and thickness of the samples. The size of the skin layer pores (sample size: 50) was measured, using the Fiji[33] distribution of ImageJ,[34] and plotted as a histogram (Fig. S1 in the ESI†). These measurements were averaged to give the skin layer pore size of a given sample. The thickness of samples was averaged from three measurements of the thickness from SEM images.

Water permeability

The water permeability of the membranes was investigated using a bespoke dead-end filtration set-up, shown in Fig. 2. Membrane samples were cut into discs, by hand, with a diameter larger than 43 mm so that they could be inserted into the set-up. The flow-rate of water through the sample membranes was recorded at a constant pressure of 1 bar supplied using compressed air to a water-filled pressure vessel. The flow-rate was found by measuring the mass of water that passed through the sample once a steady flow-rate was reached. This was repeated three times per sample to generate reliable data. At the start of the experiment, the initial flow-rate was slower than the steady-state due the time required to fill the membrane and set-up with water. The steady-state flow-rate was used to calculate the permeability of the membrane using Darcy's law:

$$Q = \frac{\kappa A \Delta P}{\eta L} \tag{1}$$

where Q is the flow-rate through the membrane, κ is the permeability of the membrane, A is the area of the sample that water passes through, and L is the sample thickness. The viscosity of the water, η, was taken as 1 mPa s.

Water contact angle

The hydrophilicity of the membrane surfaces was investigated by measuring the water contact angle using an FTA 1000 C Class Drop Shape Contact Angle Tensiometer, which uses the sessile droplet method.[35] Measurements were repeated five times per sample. Both sides of the same membrane were investigated to compare differences in the water hydrophilicity with the microstructure. The water contact angle, plotted against time, initially showed large changes before stabilising. This stabilisation point was determined by using a moving gradient over a 30-point range (corresponding to 3 seconds). This gradient tends to zero as the value stabilises. A threshold value of 1.2 was chosen as the point where stabilisation was determined to have occurred. All points from all repeats after the stabilisation point had been reached were then used to determine the water contact angle of that sample. All experiments were repeated five times. We note that the permeability
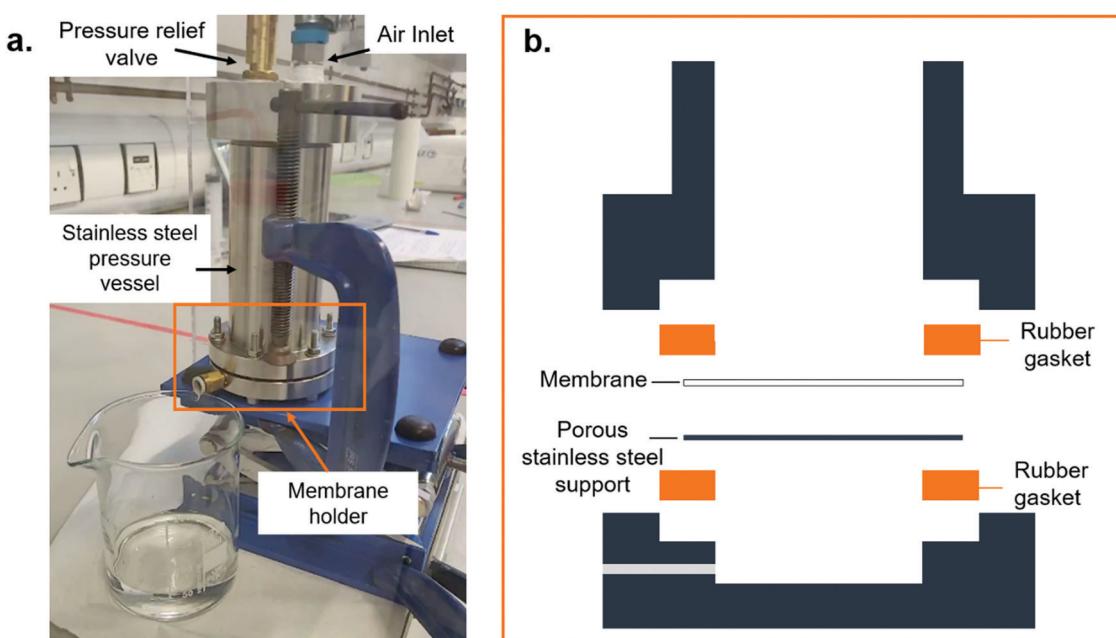
Fig. 2 (a) Photograph of the permeability testing rig in use. (b) Close-up schematic of the sample-holding chamber. A stainless steel pressure vessel is filled with water above a membrane sample. This is then pressurized using an air-line to push water through the sample. The mass of the water can be measured after a known time at a given pressure to give a flow rate.

of the samples led to fluctuations in the water contact angle as the water penetrates the sample.

Removal of the PABA template

The effect on the microstructure of removing the PABA template post-membrane formation was also examined. To determine the amount of PABA removed, samples of both control and PABA-containing membranes, of approximately 35 mg, were weighed and placed into ethanol (25 ml). After a set time interval, an aliquot (3 ml) was removed and replaced with clean ethanol. This process was repeated for the duration of the experiment (2 days in total), after which the eluent was orange in coloration for the test samples and colourless for the control samples. The eluent was diluted by a factor of 100 and its UV/Vis absorption spectrum was measured. The absorbance at λ_{abs} = 324 nm was compared against a calibration Beer–Lambert plot for PABA in ethanol to determine the concentration of eluted additive.

Results and discussion

Membrane fabrication

Membranes in this work were prepared using the NIPS method, as illustrated in Fig. 1b. The stirring temperature, degas time and immersion conditions were optimised to maximise the quality of the membranes produced, including their rapid phase separation as is discussed later in this section. The degas

time (15 minutes) was necessary to remove any air bubbles present in the viscous precursor solution prior to membrane formation, which would otherwise result in unwanted holes. Membranes were prepared using either F127 as a primary pore template (control sample) or a combination of F127 and PABA as a nanostructuring agent (test sample). The optimised procedure resulted in reproducible membranes with the same microstructure at both the 50 μm and the sub-micron scales. The concentration of PABA was fixed at 15 wt% as lower concentrations visually had less of an effect on the nanostructure. Higher concentrations of additives did not produce castable solutions and were not studied further. All samples were prepared using DMF as a solvent for the polymer/additive mixture, to eliminate any variations in the procedure due to the solvent. Based on the Hansen total solubility parameters, DMF is an excellent solvent for PES (24.9 MPa$^{0.5}$ and 24.4 MPa$^{0.5}$, respectively),[36] while water is a non-solvent (47.8 MPa$^{0.5}$).[36]

Fig. 3 shows the macro-, micro- and nanostructural appearance of the control and test films. At the macroscopic level (Fig. 3a), the control films are opaque, white and shiny in appearance, while the test samples are stained orange by the PABA additive. Cross-sectional analysis by SEM of the microstructure of the control sample reveals that the membrane is asymmetric (Fig. 3b); a skin layer, containing dense spherical pores on the nanometre scale, is observed on the top side that forms at the solution–water interface (Fig. 3c), which transitions into vertical finger-like macropores within the bulk membrane.
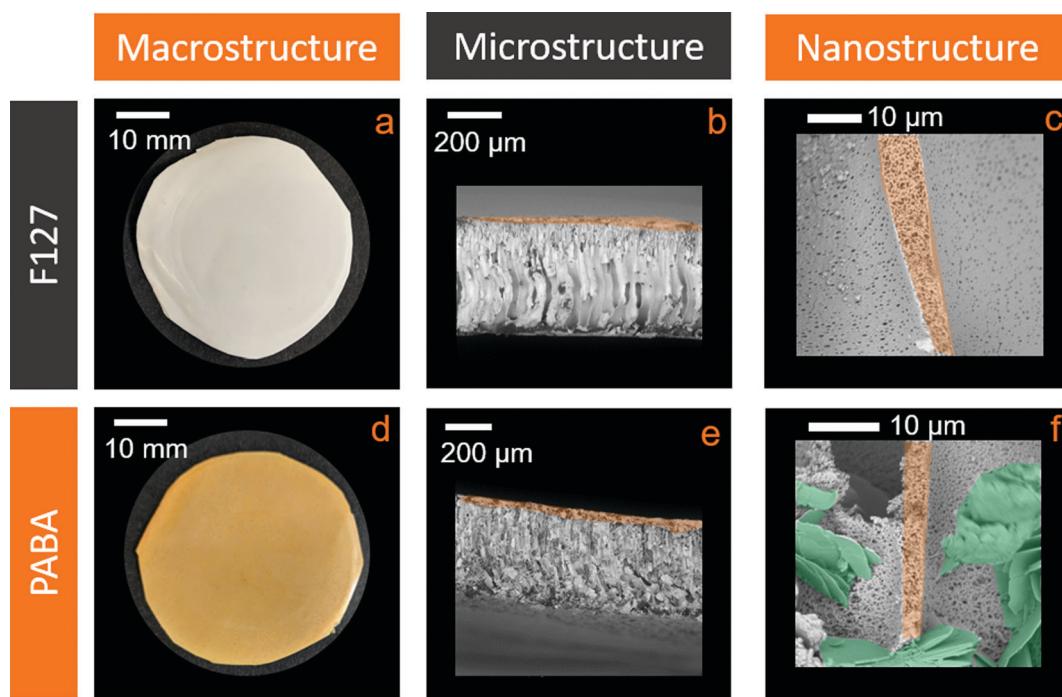
Fig. 3 Photographs and scanning electron microscope images of control and test membranes. (a and d) Give a macroscopic view of a control membrane and test membrane containing PABA, respectively. (b) Shows the finger-like pore microstructure of a control membrane, which exhibits poor nanoscale connectivity within the skin layer, highlighted in orange, and within the finger-like pore walls (c). These images contrast with the test membrane (e and f), which shows the presence of additional flakes at the 10 μm scale, shown in green, and the emergence of a fibrous nanostructure at the sub-micron scale, within the skin layer and finger-like pore walls.

786 | Mater. Chem. Front., 2021, 5, 783–791

This journal is © The Royal Society of Chemistry and the Chinese Chemical Society 2021

The membrane microstructure arises during the phase-separation process that takes place during membrane formation. As the precursor solvent and bulk non-solvent are miscible, the non-solvent infiltrates into the solution, changing the effective concentration of the polymer such that it is no longer stable in solution and it phase separates by nucleation and growth to form a solid. This process forms nuclei of a polymer-lean phase, which later develop into pores within a matrix of polymer-rich phase, resulting in the macroporous membrane desired in this work, and avoiding the sponge-like microstructure more typical of reverse osmosis membranes.[37] Under these conditions, the F127 surfactant forms micelles which act as physical stabilisers that prevent the nuclei from collapsing as they form, allowing them to develop further into pores.[20] The skin layer and the material between the finger-like macropores appears to be nanostructured in nature, showing many isolated, spheroidal pores with low connectivity and diameters of approximately 1 μm, as seen in Fig. 3c. We postulate that fast nucleation occurs initially at the solution–water interface resulting in the formation of the observed small, closely packed pores in the skin layer. This lowers the diffusivity of water through the skin layer as the bulk of the membrane precipitates, leading to the formation of vertical finger-like pores, along the concentration gradient of the water. This is vertical in relation to the sample due to the geometry used. We note that while these finger-like pores are commonly observed for membranes formed by NIPS,[20,21] to the best of our knowledge, the nanostructure in the skin layer has not been previously investigated in detail.

In the test sample, the addition of PABA to the initial casting solution allows templating of both the primary and secondary pore structure. At the 10 μm level, the appearance of flakes within the microstructure is apparent, in addition to the vertical finger-like pores found in the control membranes (Fig. 3e). The nanostructure is observed to be more fibrous and appears to exhibit a higher pore connectivity, while maintaining a similar feature size as the control membrane (Fig. 3f). If present, the increased pore connectivity should also give rise to a desirable increase in membrane permeability.

Extraction of PABA additive

PABA molecules interact poorly with the hydrophobic PES and more strongly with water, resulting in the partial leaching of PABA into the water bath when the membranes are immersed during manufacturing. This leaching is detected by the faint yellow coloration of the water during the fabrication process. Moreover, the flakes observed in the membrane microstructure (Fig. 3e) are also believed to be crystals of excess PABA, which would adversely affect its functionality as a membrane. Inadvertent leaching of PABA during service would be extremely undesirable, for instance,
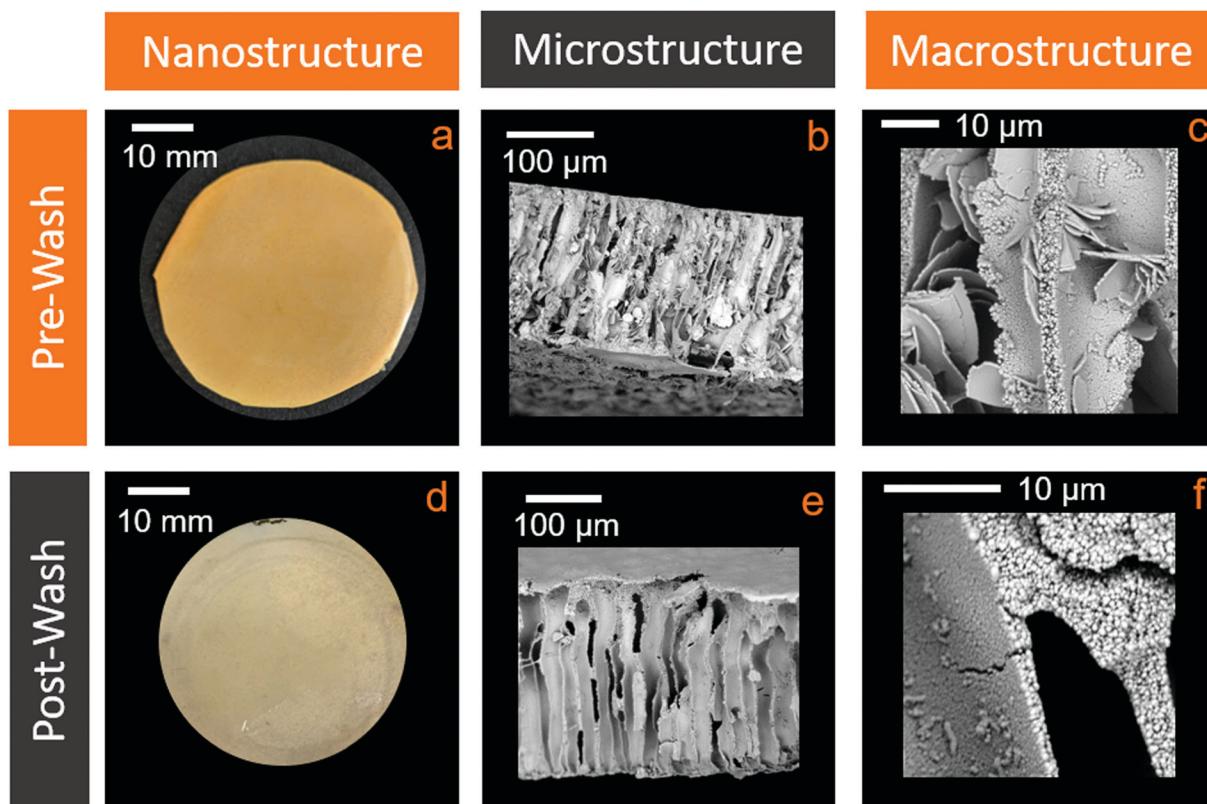
Fig. 4 Photographs and scanning electron microscope images of test membranes before and after extraction of PABA with ethanol. (a and d) Give a macroscopic view of pre-wash and post-wash samples, showing the fading of the orange colour (top side). A comparison of (b) and (e) shows the removal of the flakes in the microstructure through washing. (c) and (f) show the preservation of the fibrous nanostructure after the PABA has been removed, within the walls the frualls of the finger-like pores.
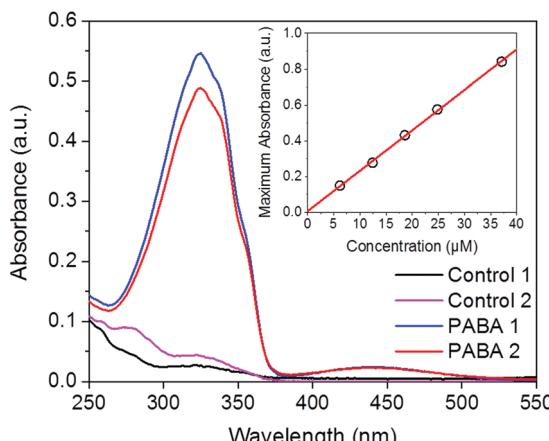
Fig. 5 Quantification of the PABA solvent-extracted from test and control membranes. UV/Vis absorption spectra of ethanol washings after two days for two control samples (black and pink lines) and two test samples (blue and red lines) are shown. The inset shows the Beer–Lambert calibration plot for PABA in ethanol ($\lambda = 324$ nm).

in a water filtration application, as this could lead to contaminated water downstream of the membrane.[38]

We therefore investigated the effect of completely removing the PABA additive on the membrane structure post-formation. To enable direct comparison of the microstructure, a membrane sample was freeze-dried and cracked into two, with one half of the sample exposed to solvent extraction and the other retained for comparison. For solvent extraction, the sample was immersed in an ethanol bath of known volume for 2 days, after which the membrane lost its orange coloration and appeared off-white in colour (Fig. 4a and d). The ethanol was regularly refreshed during this period to ensure that a concentration gradient that promoted leaching was retained throughout.

From SEM analysis, it is apparent that the large flakes originally present at the 10 μm scale were removed by the solvent extraction process (Fig. 4b and e). However, interestingly, the nanostructural porosity was unaffected, remaining fibrous and with no observable changes to the pore dimensions (Fig. 4c and f). Solvent extraction thus improves the microstructural porosity, while retaining the desirable nanoscale porosity and interconnectivity, and simultaneously greatly reduces the levels of any potentially harmful additives.

The extent of PABA removal was quantified by UV/Vis absorption spectroscopy. As shown in Fig. 5, the characteristic absorption spectra of PABA is clearly apparent in the ethanol eluent removed from the test sample. For comparison, a control membrane containing no PABA was also exposed to the same solvent extraction process; in this case PABA is absent in the corresponding absorption spectrum. A Beer–Lambert plot for PABA in ethanol was produced (Fig. 5, inset) to enable direct quantification of the PABA concentration in the ethanol eluent (absorption coefficient, $\varepsilon = 22\,580 \pm 332$ L mol^{-1} cm^{-1} at 324 nm). Following 2 days of washing, a PABA recovery of *ca.* 107% was estimated, suggesting that quantitative removal can be achieved (accounting for expected experimental error in

the concentration measurements). This introduces the possibility of recycling the PABA to template further membranes.

Contact angle measurements

The water contact angle of membranes provides a useful measure of their hydrophilicity. Many applications require a hydrophilic membrane surface; this is particularly important in water filtration applications to reduce the effect of biological fouling.[31] Fig. 6 shows representative images from water contact-angle measurements performed on both sides of control and test membranes. For the control sample, the top side of the membrane with the denser skin layer shows a higher water contact angle compared to the bottom side of the membrane that is formed in contact with the glass slide (78.83° ± 1.07° and 73.06° ± 2.87°, respectively, see Fig. 6a and b). This is attributed to the smaller pores in the dense skin layer enabling Cassie–Baxter wetting at the air/membrane/water tertiary interface.[39] The addition of PABA was observed to have a small effect on the water contact angle of the membranes, reducing the contact angle on both sides of the membrane, due to its hydrophilic presence throughout the membrane[40] (Fig. 6c and d); the contact angle of the denser skin layer decreases to 71.82° ± 2.52°, whilst the reverse side reduces more significantly to 56.96° ± 3.96°. Removal of the PABA leads to little change in contact angle on the dense skin layer (71.82° ± 2.52° to 69.67° ± 12.39°, see Fig. 6e). However, this removal has a much greater effect on the reverse side of the membrane (Fig. 6f), with the
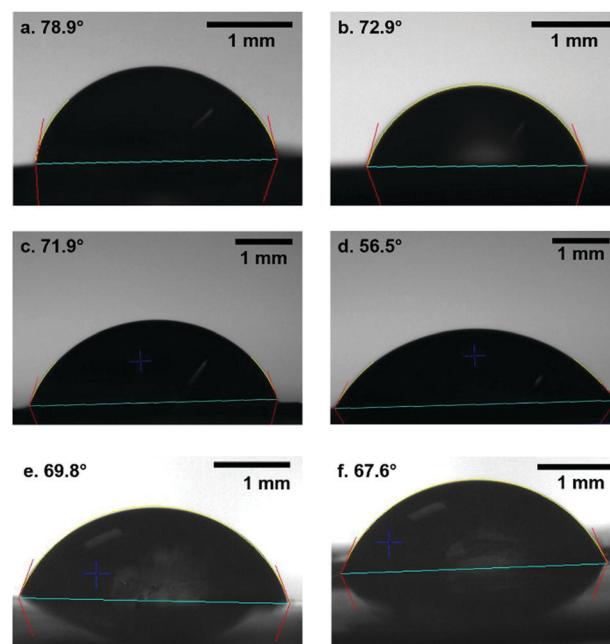

Fig. 6 Water droplet contact angle images for control and test membranes. (a) Control membrane, top-side (dense skin layer). (b) Control membrane, bottom-side (lenticular pore layer). (c) PABA-containing membrane, top-side (dense skin layer). (d) PABA-containing membrane, bottom-side (lenticular pore layer). (e) PABA-containing membrane after PABA removal, top-side (dense skin layer). (f) PABA-containing membrane after PABA removal, bottom-side (lenticular pore layer).

788 | *Mater. Chem. Front.*, 2021, **5**, 783–791

This journal is © The Royal Society of Chemistry and the Chinese Chemical Society 2021

Table 1 Performance comparison of PES ultrafiltration membranes

Ref.	Casting solution composition (wt%)	Testing pressure (bar)	Flow rate (l (m² h)⁻¹)	Notes
Present study	PES (18), F127 (9), DMF (73)	1	22.8	Skin-layer pore diameter: 220 nm (Fig. S1 in ESI)
Present study	PES (18), F127 (9), PABA (15), DMF (57)	1	54.6	Skin-layer pore diameter: 188 nm (Fig. S1 in ESI)
Present study	PES (18), F127 (9), PABA (15), DMF (57)	1	220.1	PABA removed from final membrane
21	PES (18), F127 (9), PEG^a (15), DMF (57)	1	110	Fouling reduction with increasing F127 content
20	PES (18), F127 (18), DMF (64)	1	209.1	Pore size increases with higher F127 content
30	PES (17.9), PVP^b (0.18), PA-6^c (0.18), DMAc^d (81.7)	4	40.9	Mean pore size: 10.11 nm
41	PES (15.12), SPSf^e (2.88), PEG^f (24), DMAc^g (58)	1	1467.0	Sponge-like pores Surface pore size: 22.3 nm

^{a} PEG: poly(ethylene glycol)2000. ^{b} PVP: poly(vinyl pyrrolidone). ^{c} PA-6: anthracene functionalized poly(amide). ^{d} DMAc: dimethylacetamide. ^{e} SPSf: sulfonated poly(sulfone). ^{f} PEG: poly(ethylene glycol)20 000. ^{g} DMAc: N,N-dimethylacetamide.

contact angle returning to a value similar to that of the control membrane ($68.13° \pm 13.76°$). This suggests that the presence of PABA within the membrane is responsible for the reduction in contact angle from control membranes, and can be rationalised by the presence of the hydrophilic carboxylic acid group present in PABA.

Membrane permeability

High permeability at a given pore size is typically a desirable property for most membrane applications. In this work, permeability was measured using a bespoke dead-end filtration setup as shown in Fig. 2. This set-up uses a fluid vessel, pressurised using compressed air. The fluid is forced through the sample being tested for a known time and the mass of this fluid recorded. This gives a flow-rate that can be compared between membranes. The rig allows the testing pressure and testing fluid to be varied if desired. A pressure of 1 bar was chosen in this work to prevent membrane damage or inadvertent extraction of the PABA additive during testing. Water was chosen as the permeability medium. Using this set-up, the flow-rate of the control membranes was found to be 22.8 ± 4.3 l (m² h)⁻¹, leading to a permeability of 3.97 ± 0.75 nm² for a skin-layer pore diameter of 220 ± 116 nm, as observed by SEM (Fig. S1 in ESI†). Although the membrane thickness was accounted for in the permeability calculations, we note that the asymmetric nature of the membranes may result in the permeability having a non-linear relationship to the bulk thickness since the smallest pores will make a more significant contribution. The test samples in which the PABA was retained, exhibited a 95% increase in flow rate to 54.6 ± 2.3 l (m² h)⁻¹, giving a permeability, accounting for membrane thickness, of 7.73 ± 0.33 nm², at a comparable skin-layer pore diameter of 188 ± 71 nm. We note that despite the fairly low flow pressure, it was observed that the eluent from these samples took on a faint yellow colour, suggesting some of the PABA had in fact leached out. However, the test samples exposed to ethanol extraction (*i.e.* the PABA was fully removed prior to measurement) displayed a dramatically increased flow rate of 220 ± 66 l (m² h)⁻¹, corresponding to a permeability of 31.2 ± 9.37 nm², an increase of 300% over the compared to the test samples containing PABA. This is attributed to the removal of the PABA flakes from the microstructure, leading to less obstacles in the permeation pathway. These flow-rates compare favourably to previous reports, including those using F127 to give a similar macropore structure to our work, even though they show a thinner skin layer,[20,21] as presented in Table 1.

Conclusions

We have demonstrated a new dual-template approach using the NIPS method to produce a controllable, hierarchical pore structure within PES membranes. The polymeric amphiphile F127 assembles into micelles which stabilize the formation of finger-like pores at the 10 μm scale, while the molecular additive PABA increases the connectivity of the smaller pores at the 1 μm level. This increase in connectivity has the effect of increasing the permeability of the membrane without compromising pore size. Ethanol extraction has been demonstrated as an excellent approach to quantitatively remove PABA from the resultant membranes. This process preserves the more fibrous low-level microstructure, while enabling removal of both the unwanted orange coloration and the crystalline flakes of PABA which block the larger pores. This has a striking effect on the membrane permeability, with PABA-templated membranes exhibiting a 95% increase in permeability compared to the control sample, which jumps to a further 300% increase following solvent extraction. Moreover, the PABA additive can then be recovered and recycled in further membrane production. This work demonstrates that the dual-template approach, as part of the NIPS process, can be used to fabricate membranes with a hierarchical pore structure that exhibit increased pore connectivity. Further studies are currently underway to understand how this pore connectivity influences the specific surface area. The process describe here allows for templating at the micron scale, using mild, simple processing conditions. This is advantageous when compared to other templating methods, such as block-copolymer templating[42,43] or particle-guided spinodal decomposition,[44] which require careful control of humidity, evaporation time and template composition to successfully template the desired microstructure, using a multi-step method. The controllable pore structure developed in this work results in properties that are valuable for a variety of applications, for example in membranes for water purification[45] or solar steam generation,[46–48] where the increased connectivity allows greater contact of the permeate and the active membrane surface.

This journal is © The Royal Society of Chemistry and the Chinese Chemical Society 2021

Mater. Chem. Front., 2021, **5**, 783–791 | **789**

Conflicts of interest

There are no conflicts to declare.

Acknowledgements

Notes and references

1 C. Duan, R. Kee, H. Zhu, N. Sullivan, L. Zhu, L. Bian, D. Jennings and R. O'Hayre, Highly efficient reversible protonic ceramic electrochemical cells for power generation and fuel production, *Nat. Energy*, 2019, **4**, 230–240.

2 M. A. Shannon, P. W. Bohn, M. Elimelech, J. G. Georgiadis, B. J. Mariñas and A. M. Mayes, Science and technology for water purification in the coming decades, *Nature*, 2008, **452**, 301–310.

3 P. S. Zhong, N. Widjojo, T. S. Chung, M. Weber and C. Maletzko, Positively charged nanofiltration (NF) membranes via UV grafting on sulfonated polyphenylenesulfone (sPPSU) for effective removal of textile dyes from wastewater, *J. Membr. Sci.*, 2012, **417–418**, 52–60.

4 R. E. Sousa, J. Nunes-Pereira, C. M. Costa, M. M. Silva, S. Lanceros-Méndez, J. Hassoun, B. Scrosati and G. B. Appetecchi, Influence of the porosity degree of poly(vinylidene fluoride-*co*-hexafluoropropylene) separators in the performance of Li-ion batteries, *J. Power Sources*, 2014, **263**, 29–36.

5 D. Song, J. Xu, Y. Fu, L. Xu and B. Shan, Polysulfone/ sulfonated polysulfone alloy membranes with an improved performance in processing mariculture wastewater, *Chem. Eng. J.*, 2016, **304**, 882–889.

6 X. Liu, S. He, G. Song, H. Jia, Z. Shi, S. Liu, L. Zhang, J. Lin and S. Nazarenko, Proton conductivity improvement of sulfonated poly(ether ether ketone) nanocomposite membranes with sulfonated halloysite nanotubes prepared via dopamine-initiated atom transfer radical polymerization, *J. Membr. Sci.*, 2016, **504**, 206–219.

7 B. S. Lalia, E. Guillen-Burrieza, H. A. Arafat and R. Hashaikeh, Fabrication and characterization of polyvinylidenefluoride-*co*-hexafluoropropylene (PVDF-HFP) electrospun membranes for direct contact membrane distillation, *J. Membr. Sci.*, 2013, **428**, 104–115.

8 N. Widjojo, T. S. Chung, M. Weber, C. Maletzko and V. Warzelhan, A sulfonated polyphenylenesulfone (sPPSU) as the supporting substrate in thin film composite (TFC) membranes with enhanced performance for forward osmosis (FO), *Chem. Eng. J.*, 2013, **220**, 15–23.

9 A. Lee, J. W. Elam and S. B. Darling, Membrane materials for water purification: design, development, and application, *Environ. Sci.: Water Res. Technol.*, 2016, **2**, 17–42.

10 M. Ulbricht, O. Schuster, W. Ansorge, M. Ruetering and P. Steiger, Influence of the strongly anisotropic cross-section morphology of a novel polyethersulfone microfiltration membrane on filtration performance, *Sep. Purif. Technol.*, 2007, **57**, 63–73.

11 M. A. Alaei Shahmirzadi, S. S. Hosseini, G. Ruan and N. R. Tan, Tailoring PES nanofiltration membranes through systematic investigations of prominent design, fabrication and operational parameters, *RSC Adv.*, 2015, **5**, 49080–49097.

12 A. Figoli, T. Marino, S. Simone, E. Di Nicolò, X.-M. Li, T. He, S. Tornaghi and E. Drioli, Towards non-toxic solvents for membrane preparation: a review, *Green Chem.*, 2014, **16**, 4034.

13 N. L. Le and S. P. Nunes, Materials and membrane technologies for water and energy sustainability, *Sustainable Mater. Technol.*, 2016, **7**, 1–28.

14 H. Susanto and M. Ulbricht, Characteristics, performance and stability of polyethersulfone ultrafiltration membranes prepared by phase separation method using different macromolecular additives, *J. Membr. Sci.*, 2009, **327**, 125–135.

15 W. Chen, M. Wei and Y. Wang, Advanced ultrafiltration membranes by leveraging microphase separation in macrophase separation of amphiphilic polysulfone block copolymers, *J. Membr. Sci.*, 2017, **525**, 342–348.

16 W.-L. Hung, D.-M. Wang, J.-Y. Lai and S.-C. Chou, On the initiation of macrovoids in polymeric membranes – effect of polymer chain entanglement, *J. Membr. Sci.*, 2016, **505**, 70–81.

17 C. G. Ferreira, V. F. Cardoso, A. C. Lopes, G. Botelho and S. Lanceros-Méndez, Tailoring microstructure and physical properties of poly(vinylidene fluoride–hexafluoropropylene) porous films, *J. Mater. Sci.*, 2015, **50**, 5047–5058.

18 Y.-Q. Wang, Y.-L. Su, Q. Sun, X.-L. Ma and Z.-Y. Jiang, Generation of anti-biofouling ultrafiltration membrane surface by blending novel branched amphiphilic polymers with polyethersulfone, *J. Membr. Sci.*, 2006, **286**, 228–236.

19 G. R. Guillen, Y. Pan, M. Li and E. M. V. Hoek, Preparation and Characterization of Membranes Formed by Nonsolvent Induced Phase Separation: A Review, *Ind. Eng. Chem. Res.*, 2011, **50**, 3798–3817.

20 W. Zhao, Y. Su, C. Li, Q. Shi, X. Ning and Z. Jiang, Fabrication of antifouling polyethersulfone ultrafiltration membranes using Pluronic F127 as both surface modifier and pore-forming agent, *J. Membr. Sci.*, 2008, **318**, 405–412.

21 Y.-Q. Wang, T. Wang, Y. Su, F.-B. Peng, H. Wu and Z.-Y. Jiang, Remarkable reduction of irreversible fouling and improvement of the permeation properties of poly(ether sulfone) ultrafiltration membranes by blending with Pluronic F127, *Langmuir*, 2005, **21**, 11856–11862.

22 M. Amirilargani, E. Saljoughi and T. Mohammadi, Improvement of permeation performance of polyethersulfone (PES) ultrafiltration membranes via addition of Tween-20, *J. Appl. Polym. Sci.*, 2010, **115**, 504–513.

23 N. Arahman, T. Maruyama, T. Sotani and H. Matsuyama, Fouling Reduction of a Poly(ether sulfone) Hollow-Fiber Membrane with a Hydrophilic Surfactant Prepared via

Non-Solvent-Induced Phase Separation, *J. Appl. Polym. Sci.*, 2009, **111**, 1653–1658.

24 N. A. Rahman, T. Sotani and H. Matsuyama, Effect of the Addition of the Surfactant Tetronic 1307 on Poly(ether sulfone) Porous Hollow-Fiber Membrane Formation, *J. Appl. Polym. Sci.*, 2008, **108**, 3411–3418.

25 B. Jiang, B. Wang, L. Zhang, Y. Sun, X. Xiao, N. Yang and H. Dou, Effect of Tween 80 on morphology and performance of poly(L-lactic acid) ultrafiltration membranes, *J. Appl. Polym. Sci.*, 2017, **134**, 44428.

26 D. Zhao, J. Feng, Q. Huo, N. Melosh, G. H. Fredrickson, B. F. Chmelka and G. D. Stucky, Triblock copolymer syntheses of mesoporous silica with periodic 50 to 300 angstrom pores, *Science*, 1998, **279**, 548–552.

27 M. Kruk, M. Jaroniec, C. H. Ko and R. Ryoo, Characterization of the porous structure of SBA-15, *Chem. Mater.*, 2000, **12**, 1961–1968.

28 A. Jalali, A. Shockravi, V. Vatanpour and M. Hajibeygi, Preparation and characterization of novel microporous ultrafiltration PES membranes using synthesized hydrophilic polysulfide-amide copolymer as an additive in the casting solution, *Microporous Mesoporous Mater.*, 2016, **228**, 1–13.

29 Y. Feng, G. Han, T. S. Chung, M. Weber, N. Widjojo and C. Maletzko, Effects of polyethylene glycol on membrane formation and properties of hydrophilic sulfonated polyphenylenesulfone (sPPSU) membranes, *J. Membr. Sci.*, 2017, **531**, 27–35.

30 A. Shockravi, V. Vatanpour, Z. Najjar, S. Bahadori and A. Javadi, A new high performance polyamide as an effective additive for modification of antifouling properties and morphology of asymmetric PES blend ultrafiltration membranes, *Microporous Mesoporous Mater.*, 2017, **246**, 24–36.

31 B. Vatsha, J. C. Ngila and R. M. Moutloali, Preparation of antifouling polyvinylpyrrolidone (PVP 40K) modified polyethersulfone (PES) ultrafiltration (UF) membrane for water purification, *Phys. Chem. Earth*, 2014, **67–69**, 125–131.

32 P. Anastas and J. Warner, *Green Chemistry: Theory and Practice*, Oxford University Press, 2000.

33 J. Schindelin, I. Arganda-Carreras, E. Frise, V. Kaynig, M. Longair, T. Pietzsch, S. Preibisch, C. Rueden, S. Saalfeld, B. Schmid, J. Y. Tinevez, D. J. White, V. Hartenstein, K. Eliceiri, P. Tomancak and A. Cardona, Fiji: An open-source platform for biological-image analysis, *Nat. Methods*, 2012, **9**, 676–682.

34 M. D. Abràmoff, P. J. Magalhães and S. J. Ram, Image processing with imageJ, *Biophotonics Int.*, 2004, **11**, 36–41.

35 *Applied Surface Thermodynamics*, ed. R. David, A. W. Neumann and Y. Zuo, CRC Press, Boca Raton, FL, 2nd edn, 2010, pp. 284–288.

36 C. M. Hansen, *Hansen Solubility Parameters: A User's Handbook*, CRC Press, 2nd edn, 2007.

37 C. Barth, M. C. Gonçalves, A. T. N. Pires, J. Roeder and B. A. Wolf, Asymmetric polysulfone and polyethersulfone membranes: Effects of thermodynamic conditions during formation on their performance, *J. Membr. Sci.*, 2000, **169**, 287–299.

38 4-(Phenylazo)benzoic acid Safety Data Sheet, https://www.sigmaaldrich.com/MSDS/MSDS/DisplayMSDSPage.do?country=GB&language=en&productNumber=479624&brand=ALDRICH, accessed 20 August 2020.

39 D. J. Johnson, D. L. Oatley-Radcliffe and N. Hilal, State of the art review on membrane surface characterisation: Visualisation, verification and quantification of membrane properties, *Desalination*, 2018, **434**, 12–36.

40 G. B. Demirel, N. Dilsiz, M. Akmak and T. Aykara, Molecular design of photoswitchable surfaces with controllable wettability, *J. Mater. Chem.*, 2011, **21**, 3189–3196.

41 S. Li, Z. Cui, L. Zhang, B. He and J. Li, The effect of sulfonated polysulfone on the compatibility and structure of polyethersulfone-based blend membranes, *J. Membr. Sci.*, 2016, **513**, 1–11.

42 Y. M. Li, Q. Zhang, J. R. Álvarez-Palacio, I. F. Hakem, Y. Gu, M. R. Bockstaller and U. Wiesner, Effect of humidity on surface structure and permeation of triblock terpolymer derived SNIPS membranes, *Polymer*, 2017, **126**, 368–375.

43 W. A. Phillip, R. Mika Dorin, J. Werner, E. M. V. Hoek, U. Wiesner and M. Elimelech, Tuning structure and properties of graded triblock terpolymer-based mesoporous and hybrid films, *Nano Lett.*, 2011, **11**, 2892–2900.

44 M. Stucki, M. Loepfe and W. J. Stark, Porous Polymer Membranes by Hard Templating – A Review, *Adv. Eng. Mater.*, 2018, **20**, 1–18.

45 S. Ling, K. Jin, D. L. Kaplan and M. J. Buehler, Ultrathin Free-Standing Bombyx mori silk Nanofibril Membranes, *Nano Lett.*, 2016, **16**, 3795–3800.

46 J. Yang, Y. Pang, W. Huang, S. K. Shaw, J. Schiffbauer, M. A. Pillers, X. Mu, S. Luo, T. Zhang, Y. Huang, G. Li, S. Ptasinska, M. Lieberman and T. Luo, Functionalized Graphene Enables Highly Efficient Solar Thermal Steam Generation, *ACS Nano*, 2017, **11**, 5510–5518.

47 H. Ghasemi, G. Ni, A. M. Marconnet, J. Loomis, S. Yerci, N. Miljkovic and G. Chen, Solar steam generation by heat localization, *Nat. Commun.*, 2014, **5**, 1–7.

48 F. Zhao, X. Zhou, Y. Shi, X. Qian, M. Alexander, X. Zhao, S. Mendez, R. Yang, L. Qu and G. Yu, Highly efficient solar vapour generation via hierarchically nanostructured gels, *Nat. Nanotechnol.*, 2018, **13**, 489–495.

This journal is © The Royal Society of Chemistry and the Chinese Chemical Society 2021

Mater. Chem. Front., 2021, **5**, 783–791 | **791**